Arabian Journal of Chemistry (2020) 13, 5229–5240

King Saud University

Arabian Journal of Chemistry

www.ksu.edu.sa
www.sciencedirect.com

ORIGINAL ARTICLE

Highly efficient adsorption of Pb(II) by cubic nanocrystals in aqueous solution: Behavior and mechanism

Dan Ma [a], Xuegang Zou [a], Ruobai Li [a], Ping Chen [a,b], Yalan Wang [a], Tiansheng Chen [a], Qianxin Zhang [a], Haijin Liu [c], Yuping Chen [a], Wenying Lv [a,*], Yiping Feng [a], Guoguang Liu [a]

[a] *School of Environmental Science and Engineering, Guangdong University of Technology, Guangzhou 510006, China*
[b] *School of Environment, Tsinghua University, Beijing 100084, China*
[c] *Key Laboratory for Yellow River & Huaihe River Water Environment and Pollution Control, School of Environment, Henan Normal University, Xinxiang 453007, China*

Received 4 January 2020; accepted 25 February 2020
Available online 4 March 2020

KEYWORDS

Mn-Fe Prussian blue analogue;
$K_2Mn[Fe(CN)_6]$ nanocrystal;
Lead;
Adsorption;
Mechanism

Abstract As one of the most toxic heavy metal ions, lead pollution has become an urgent problem. Here, a cubic crystal nanoparticle (Prussian blue analogue, PBA), referred to as potassium manganese ferrocyanide (KMFC) was synthesized and used as a highly-effective sorbent for removing Pb(II) from aqueous solution. KMFC is a mesoporous material that has excellent ion exchange properties, which was confirmed by a series of characterizations. This paper investigated the adsorptive attributes of KMFC for lead ions in aqueous solution. The influences of temperature, contact time and pH on adsorption were studied in batch experiments. The KMFC possessed a robust adsorption capacity for resident lead ions in aqueous solution, which attained 1075.27 mg g^{-1} at room temperature (25 °C), based on the Langmuir model, which was far higher than any previously reported values. The adsorption process was well fitted to a pseudo-second-order kinetic model, as well as Langmuir and Temkin isotherm models, and was endothermic and spontaneous on the basis of thermodynamic analysis. The adsorption of Pb(II) on the surface of KMFC started with electrostatic attraction, due to the electronegativity of KMFC. Further, ion exchange was the dominant mechanism in this adsorption process, which was confirmed by FTIR, XPS, and other supplementary experiments. The good chemisorption (K^+ exchange) properties of KMFC suggested that it likely has excellent prospects in applications for heavy metal ions adsorption. This study not only

* Corresponding author.
E-mail address: lvwy612@163.com (W. Lv).
Peer review under responsibility of King Saud University.

Production and hosting by Elsevier

https://doi.org/10.1016/j.arabjc.2020.02.022

provided a new perspective for the design and development of heavy metal sorbents but provided a deep insight into the mechanism of adsorption of heavy metal ions by PBA.

1. Introduction

Lead is a highly poisonous element that is naturally present in agricultural soils and ambient water bodies, which is referred to as a bio-accumulative, persistent, and toxic heavy metal (Safruk et al., 2017). The primary sources of aqueous lead contamination include heavy metal and industrial wastewaters, printing, and domestic sewage in mining areas. At high exposure concentrations, lead can cause serious brain and central nervous system impairments and death (Manawi et al., 2018). As one of the most toxic of the heavy metals, Pb(II) contamination always arouses public concern (Song et al., 2018). The severe lead contamination of surface water tends to accumulate in vegetables and seafood, which poses great threats to human health. The remediation of lead-contaminated water has emerged as an important research topic for scholars in various countries.

Currently, several methods such as solvent extraction, electrochemical separation, precipitation, membrane filtration, ion exchange, and adsorption (Mohan et al., 2017; Xiao et al., 2015), have been extensively applied for the removal of Pb (II) from aqueous media. Among these techniques, adsorption has attractive advantages such as low cost, high removal efficiency, and simple operation; thus, it is considered to be one of the most promising methods to date (Xue et al., 2016). Consequently, activated carbon (Maleki et al., 2015), mesoporous silica (Benhamou et al., 2009; Da'Na and Sayari, 2012), and inexpensive naturally-occurring lignocellulose substrates are widely employed as sorbents for the removal of heavy metals. However, these sorbents possess disadvantages, including low adsorption capacities, unfavorable selectivity, and poor regeneration, which restricts their application (Cui et al., 2019a,b). Therefore, it is critical to research and identifies new types of materials with high adsorption abilities at a low cost (Alamudy and Cho, 2018; Kang et al., 2018).

Prussian blue analogue (PBA) is a classic type of mixed-valence hexacyanoferrate, which is formed via self-assembly. The central transition metal ion of PBA serves as a metal linker, whereas a cyanide group ligand serves as an organic linker. As can be seen in Fig. 1, it possesses a cubic frame structure. Recently, PBA has attracted significant attention due to its strong potential for extensive applications, spanning the fields of catalysis, energy storage, and biomedicine. The facile synthesis, nontoxicity, cost effectiveness, easy nanoparticle size tunability, and facile surface modification of PBAs make them ideal for large-scale production and multifunctional applications.

Herein, a K-rich Mn/Fe-based Prussian blue analogue, KMFC (potassium manganese ferrocyanide) was prepared by liquid precipitation. The excellent catalytic activity of KMFC might be attributed to its nanoporous cubic morphology with a porous face-centered cubic lattice structure and low degree of crystallinity, which makes available a large population of active sites. Typically, the KMFC exhibits excellent selective adsorption properties (Alamudy and Cho, 2018; Kang et al., 2018), due to an open frame and extensive three-dimensional porous structure. This nanometric geometry provides abundant sites and transport channels for the reversible deintercalation of larger sized ions, which involves a combination of chemisorption (high K-insertion capacity) and physisorption. However, no research has been conducted to date on the adsorption of heavy metal ions by Prussian blue analogues, including KMFC.

In this work, for the first time, KMFC was employed to adsorb lead ions from an aqueous solution and achieved spectacular results. The morphologies, specific surface area, and pore size of the KMFC were investigated by various technical characterizations. Moreover, the adsorption mechanisms of Pb (II) on the KMFC and various influencing factors, including pH, ionic strength, adsorption isotherms, and adsorption kinetics were investigated.

2. Experimental

2.1. Reagents

The chemical reagents used in this study were of analytical grade or higher. Potassium ferrocyanide(II) trihydrate ($K_4Fe(CN)_6{\cdot}3H_2O$, 99%) and manganese(II) chloride tetrahydrate ($MnCl_2{\cdot}4H_2O$, >98%) were obtained from Shanghai Aladdin Biochemical Technology Co., Ltd; Potassium chloride (KCl, >99.5%) was purchased from the Shanghai Macklin Biochemical Co., Ltd.; Lead nitrate ($Pb(NO_3)_2$), absolute ethanol, NaOH, HCl, and HNO_3 were purchased from Guangzhou Chemical Reagent Factory.

2.2. Preparation of KMFC

Preparation of the KMFC material generally followed the protocol of Jiang *et al.*, although some improvements were implemented in the present paper (Jiang et al., 2017). Initially, 5 mmol of $K_4[Fe(CN)_6]$ and 15 g of KCl were dissolved in 100 mL of ultrapure water to form Solution A, while 5 mmol of $MnCl_2$ dissolving in 50 mL of ultrapure water to form Solution B. Then, Solution B was slowly dropwise (over 15 min) into solution A under constant stirring. A white suspension was formed and stirred for an additional two hours to facilitate the completion of the reaction. The solid phase was subsequently removed through centrifugation and then rinsed with ultrapure water twice, vacuum dried at 110 °C, and ground into a powder to obtain KMFC (potassium manganese ferrocyanide). Compared with Jiang et al., this study has improved the preparation time, the number of molding elution times and the drying time.

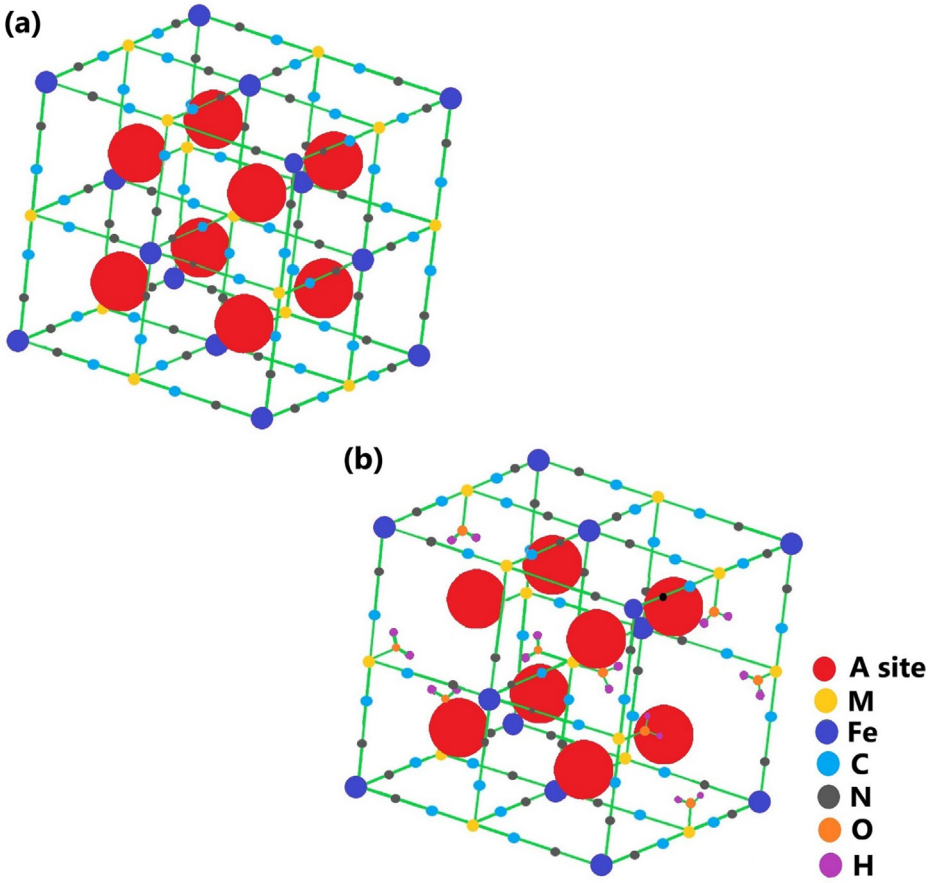

Fig. 1 Schematic diagram of the crystal structure of the Prussian blue analogue: (a) an ideal vacancy-free $A_xM[Fe(CN)_6]_{1-y}$ framework; (b) a defect-rich $A_xM[Fe(CN)_6]_{1-y} \cdot \Delta_y \cdot nH_2O$ framework. Coordinating water molecules that occupied the cavities of each of the eight sub-cubes are omitted for clarity. ($0 \leq x \leq 2$, $0 \leq y \leq 1$; A represents mobile cations, such as Li^+, Na^+, K^+ etc., M represents transition metal ions, such as Mn, Co, Ni, Cu etc., and Δ represents a $[Fe(CN)_6]$ vacancy occupied with coordinating water).

2.3. Adsorption experiments

For the isothermal adsorption experiments, different concentrations of Pb(II) solution (100–1000 mg L^{-1}, configured Pb $(NO_3)_2$, dissolved with a small amount of dilute HNO_3) (30 mL) were adsorbed with 10 mg of the sample at a pH value of 5.0 (adjusted with 0.1 mol L^{-1} NaOH) at different temperatures (298–318 K), followed by shaking for 12 h. The resulting supernatant solution was filtered and finally measured to quantify the Pb(II) concentration using a flame atomic absorption spectrophotometer(Xie et al., 2019b; Zhu et al., 2018).

The adsorption of KMFC on Pb(II) was expressed by the quantity of metal ions adsorbed in the solution. The calculation formula is:

$$q_e = \frac{(C_0 - C_e) \times V}{m} \quad (1)$$

where c_e (mg L^{-1}) is the concentration of adsorbate at equilibrium, V (L) is the volume of adsorbate, m (g) is the mass of adsorbent, and q_e (mg g^{-1}) is the adsorbed quantity at equilibrium.

2.4. Characterization of KMFC

The morphology of the KMFC powder was examined by SU8220 scanning electron microscopy (SEM; Hitach, Japan). Prior to SEM analysis, the sample was subjected to gold spray treatment to form a conductive layer on the surface. Transmission electron microscopy (TEM) images were examined by Tecnai G2 20 microscope (FEI, United States). Surface area measurements were obtained with an ASAP2020 Plus HD88 fully automatic specific surface area and porosity analyzer (Micromeritics, United States). The sample was degassed overnight under nitrogen prior to adsorption measurements. The pore distribution and volume were calculated using the adsorption branch of the N_2 isotherm based on the BJH model. The XRD pattern of the prepared sample was acquired using a D8 ADVANCE X-ray diffractometer (Bruker, Germany) to confirm the structure of the KMFC. X-ray photoelectron spectroscopy (XPS) was performed using an Escalab 250Xi instrument (Thermo Fisher, Britain). The zeta potential was measured at various pH with a Zetasizer NANO ZS (Malvern, Britain). The functional groups on the material were investigated via Fourier-transform infrared spectroscopy (FT-IR, Nicolet6700, Thermo, United States). The residual lead ions in aqueous solution were diluted to below 10 mg/L and determined with an Atomic Absorption Spectrometer (Z2000, Japan). The calibration curves of lead ions were developed from 0 to 2, 4, 6, 8, and 10 mg L-1 in a 2 vol% of concentrated HNO_3 in ultrapure water ($R^2 > 0.9995$).

3. Results and discussion

3.1. Characterization of KMFC

The morphology of the KMFC was observed via TEM and SEM. As a result, the TEM and SEM images in Fig. 2 depict that KMFC was a cubic-like crystal with a particle size of 20–30 nm. The crystal structure of the KMFC nano-cube was characterized by powder X-ray diffraction (Fig. 3a). This confirmed the monoclinic phase structure of the KMFC, as the sharp peaks confirmed that the product was well crystallized. The N_2 adsorption-desorption isotherms of the KMFC were shown in Fig. 3b. A specific Brunauer-Emmett-Teller surface area of 42.240 m^2 g^{-1} was measured for the KMFC powder. The pore size distribution curve revealed an average pore size of 100.080 Å, which was mesoporous in nature, whereas the KMFC pore volume was 0.183 m^3 g^{-1}. The Type IV isotherms with a hysteresis loop characteristic of large constricted mesopores were observed for the KMFC, which indicated a typical mesoporous structure (TIWARI et al., 2013).

Meanwhile, the zeta potential was measured to elucidate the KMFC–heavy metal interactions (Fig. 3c). The surface charge of the KMFC was negative and became more so at higher pH levels, which enhanced the electrostatic interactions that accounted for improved adsorption (Efome et al., 2018). The zeta potential of the KMFC was from −22 to −38 mV, which reflects the stability of colloidal systems. As reported in previous studies, most materials typically had an isoelectric point (pH_{PZC}), which indicated only a negative charge within a certain range in the environment (Efome et al., 2018; Xin et al., 2012). However, in contrast, the surface adsorption of negatively charged KMFC can be widely employed to adsorb cations throughout the environment (Efome et al., 2018).

3.2. Pb(II) adsorption kinetics by KMFC

Kinetics usually determine the mass transfer rate of adsorption and are considered to be one of the most important considerations (Chen et al., 2013). From Fig. 4a, the adsorption rate of KMFC increased initially, growing rapidly, and then achieved adsorption equilibrium at 180 min for Pb(II), because of the high initial Pb(II) concentration in the solution. At the onset, the abundant adsorption sites on the KMFC surface facilitated the rapid adsorption of Pb(II) at the adsorption sites (Yan et al., 2017). When the adsorption process was prolonged, both the Pb(II) concentration and the available adsorption sites were decreased, which resulted in a gradual decrease of the Pb(II) adsorption rate. Finally, the Pb(II) adsorption process reached saturation. The experimental adsorption results were analyzed and calculated by kinetic models as follows:

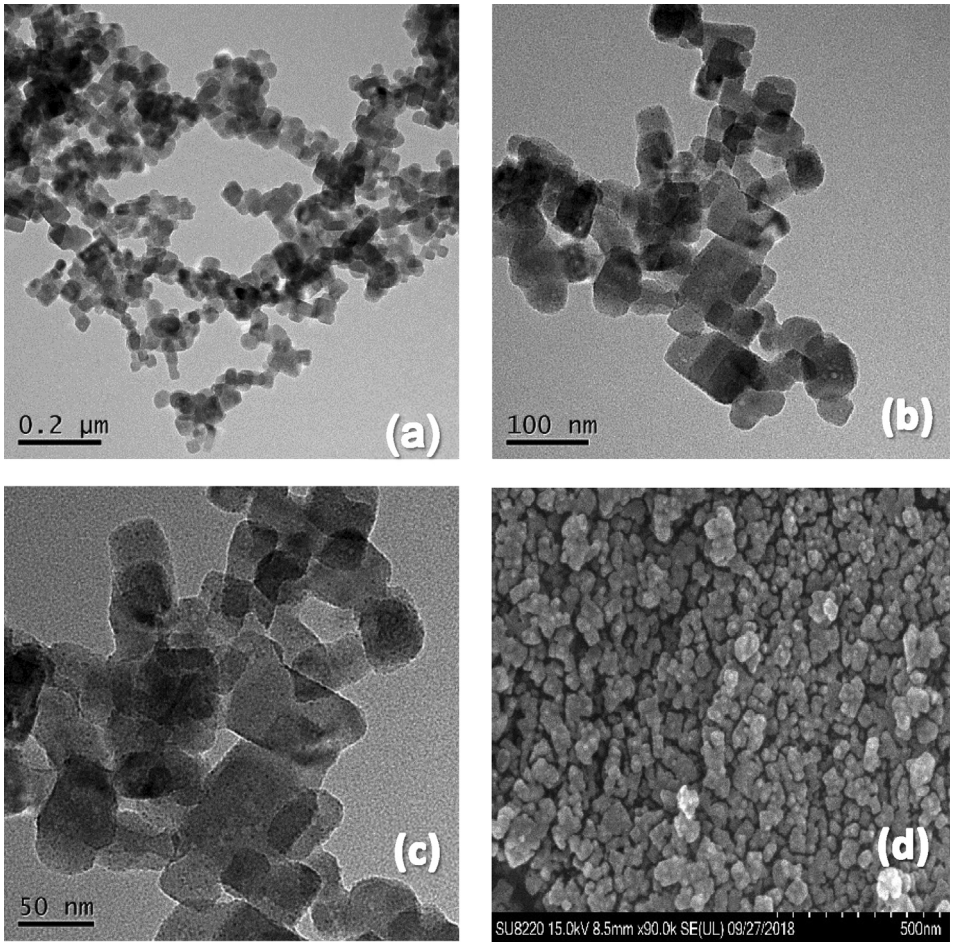

Fig. 2 TEM images (a, b, c) and SEM images (d) of the KMFC.

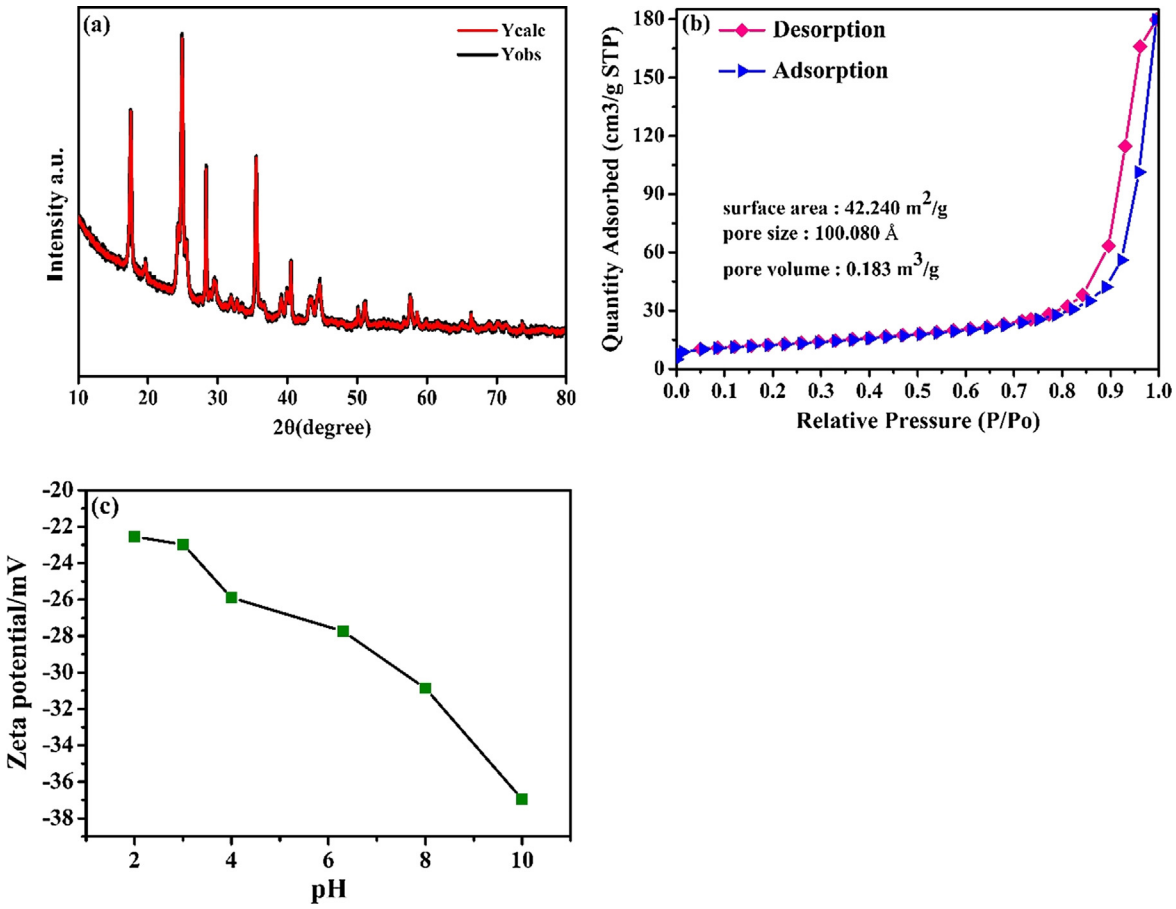

Fig. 3 (a) XRD pattern of KMFC; (b) N_2 adsorption–desorption isotherms of the KMFC; (c) Zeta potential of the KMFC.

pseudo-first-order kinetic model,

$$\ln(q_e - q_t) = lnq_e - k_{ad}\frac{t}{2.303} \quad (2)$$

pseudo-second-order kinetic model,

$$\frac{t}{q_t} = \frac{1}{kq_e^2} + \frac{t}{q_e} \quad (3)$$

and intraparticle diffusion model,

$$q_t = k_{id}t^{1/2} + C \quad (4)$$

where q_e and q_t (mg g^{-1}) are the adsorbed quantity of Pb(II) by KMFC at equilibrium and at time t (min), respectively. k_{ad} (min^{-1}) and k (mg g^{-1}·min^{-1}) are the pseudo-first-order and pseudo-second-order rate constant, respectively. k_{id}(mg g^{-1}· $min^{-0.5}$) represents the internal diffusivity constant of the particle, and C represents the boundary layer thickness, which is a constant.

Based on the calculated parameters (Table 1), the adsorption kinetic data fitted better with the pseudo-second-order kinetic mode l(R^2>0.999), as compared to the pseudo-first-order kinetic model. In addition, the q_e value (1085.78 mg g^{-1}) of Pb (II) onto KMFC calculated by the pseudo-second-order kinetic model was similar to the experiment q_{max} (1086.96 mg g^{-1}). It indicated that the adsorption process may be dominated by surface complexation or chemisorption. Moreover, chemisorption generally involves ion exchange and covalent forces and (Dan et al., 2012; Fan et al., 2017; Sun et al., 2014), which could more accurately describe the adsorption kinetics of adsorbates on sorbents.

The adsorption kinetics involves three adsorption processes: external liquid membrane diffusion, surface adsorption, and intraparticle diffusion. In order to further analyze the adsorption control mechanism and diffusion phenomenon, an intraparticle diffusion model was established. Fitting a particle diffusion model at each stage to obtain the intra-particle diffusion curve equation, the data are shown in Table 2. From Fig. 4d, the adsorption process was divided into three different stages, where the first stage was the liquid film diffusion process, followed by the intraparticle diffusion process and the adsorption saturation (Zhou et al., 2018), respectively. In summary, Pb(II) adsorption process onto KMFC was dominated by the pseudo-second-order kinetic, with intraparticle diffusion.

3.3. Pb(II) adsorption isotherms by KMFC

The equilibrium adsorption isotherm is critical in the adsorption system because it describes the balance and interaction between adsorbates and sorbents (Sharma et al., 2017). From Fig. 5a, the level of adsorption on the KMFC was increased with higher Pb(II) concentrations. The quantity of Pb(II) adsorption increased slowly as the concentration of Pb(II) attained a certain value to eventually reach saturation, which indicated that the quantity of Pb(II) adsorption onto the

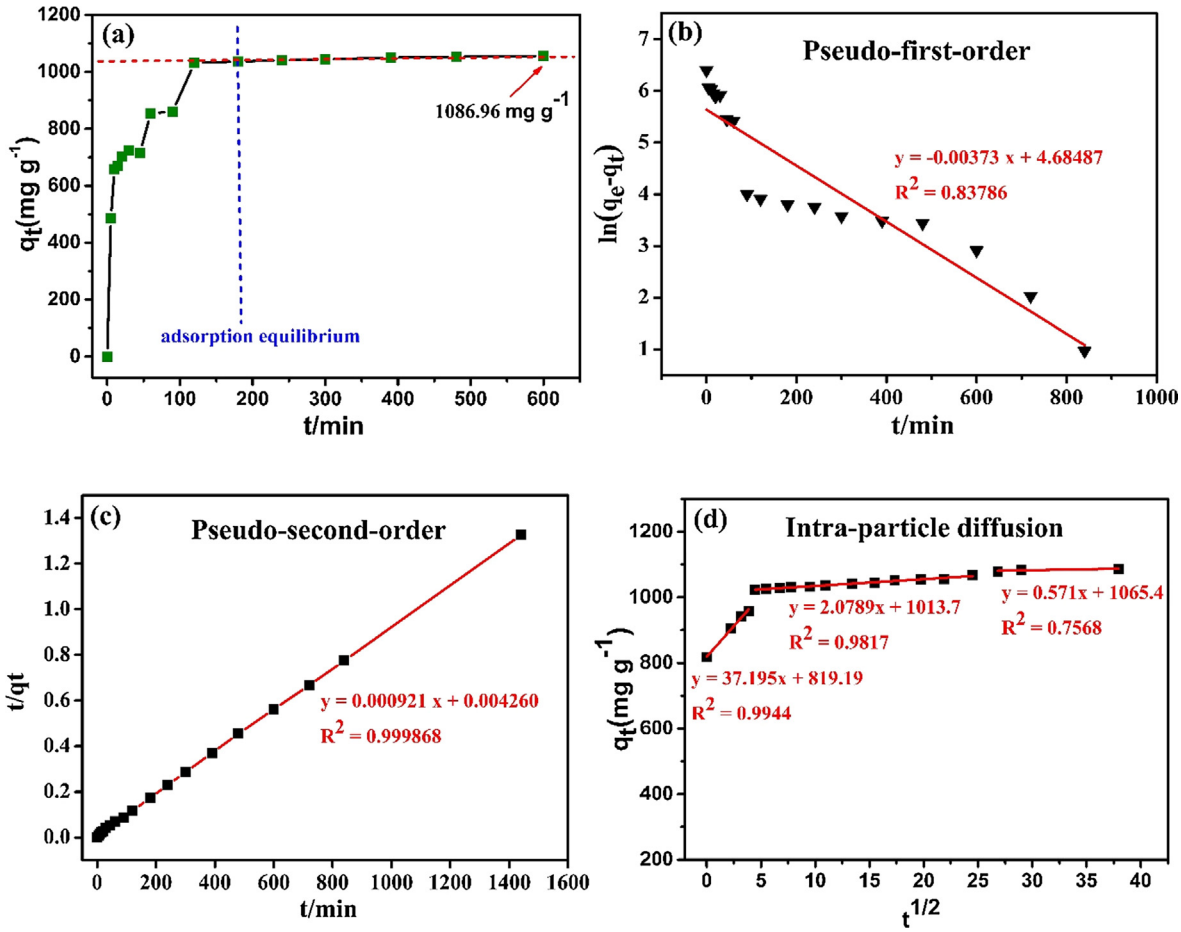

Fig. 4 (a) Effect of the contact time on adsorption of Pb(II) via KMFC (30 mL Pb(II) of 800 mg L^{-1}, 10 mg KMFC, 25 °C, pH = 5.0, 220 rpm), and the adsorption kinetics modeled with (b) pseudo-first-order, (c) pseudo-second-order and (d) intraparticle diffusion.

Table 1 Constants and correlation coefficients for the kinetics models.

Metal ion	Initial concentration	Pseudo-first-order model			Pseudo-second-order model		
	C_0 (mg·L^{-1})	q_e (mg·g^{-1})	k_{ad} (min^{-1})	R^2	q_e (mg·g^{-1})	k (mg·g^{-1}·min^{-1})	R^2
Pb(II)	800	268.097	0.01244	0.83786	1086.96	116.2791	0.99987

Table 2 Constants and correlation coefficients for intraparticle diffusion model.

Metal ion	Liquid film diffusion			Intraparticle diffusion			Equilibrium stage		
	k_{id1} (mg·g^{-1}·$min^{-0.5}$)	C_1	R_1^2	k_{id2} (mg·g^{-1}·$min^{-0.5}$)	C_2	R_2^2	k_{id3} (mg·g^{-1}·$min^{-0.5}$)	C_3	R_3^2
Pb(II)	37.195	819.195	0.9944	2.079	1013.721	0.9817	0.571	1065.424	0.7568

KMFC was related to the concentration of Pb(II) in the equilibrium solution. As the temperature was increased, the maximum level of Pb(II) adsorption increased gradually, indicating that higher temperatures benefit the adsorption process.

The Langmuir Eq. (5), Freundlich Eq. (6), Temkin Eq. (7), and Dubinin–Radushkevich (D–R, Eqs. (8)–(10)) isotherm models were proposed as the following Equations:

$$\frac{C_e}{q_e} = \frac{1}{q_{max}K_L} + \frac{C_e}{q_{max}} \tag{5}$$

$$\ln q_e = \ln K_F + \frac{\ln C_e}{n} \tag{6}$$

$$q_e = \frac{RT}{b_T} ln K_T + \frac{RT}{b_T} ln C_e \tag{7}$$

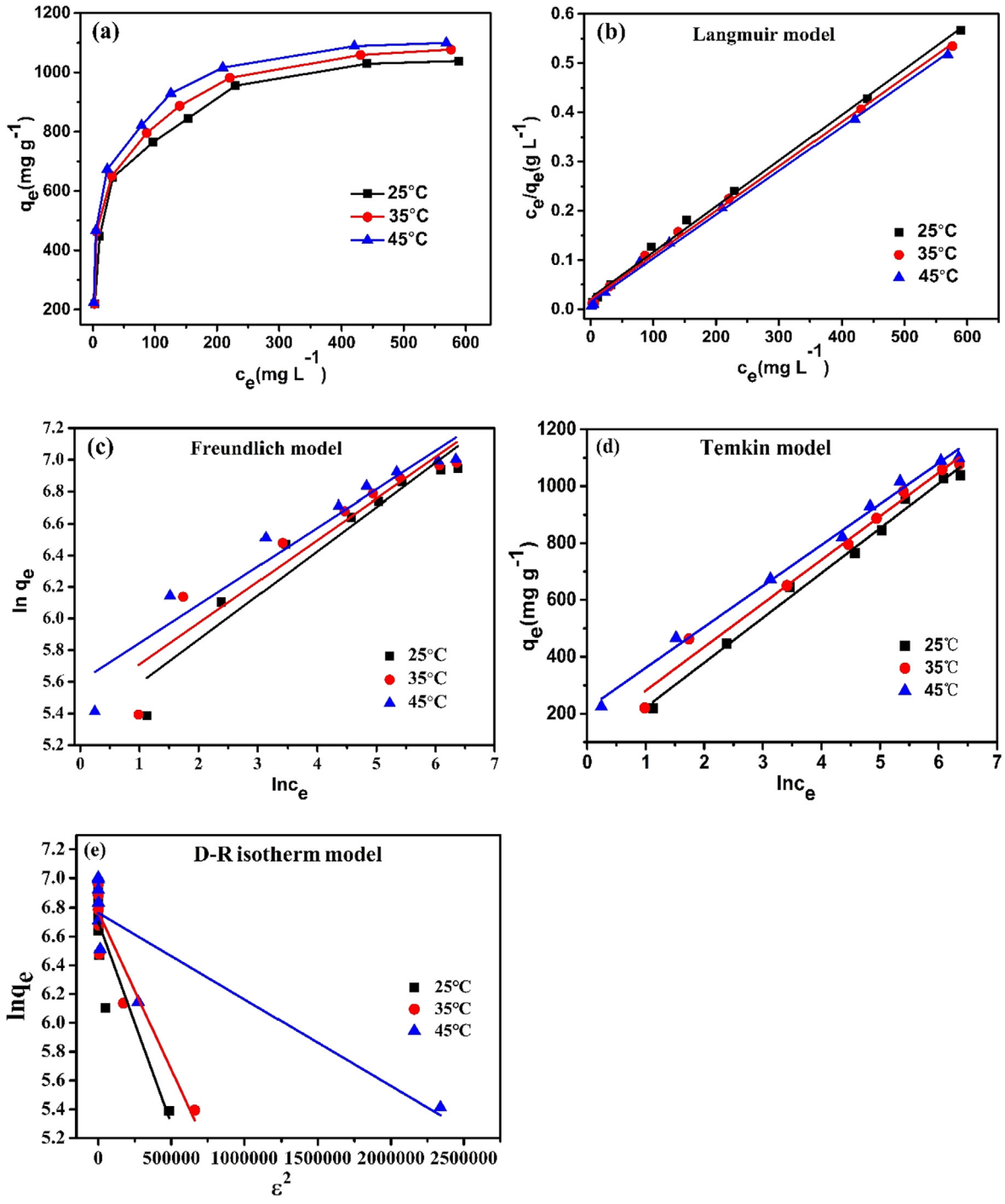

Fig. 5 (a) Adsorption isotherms of Pb(II) on the KMFC (30 mL Pb(II) per 100–1000 mg L^{-1}, 10 mg KMFC, pH = 5.0, 220 rpm, 720 min); the fitting of (b) Langmuir, (c) Freundlich, (d) Temkin, (e) D–R isotherms for Pb(II) adsorption onto the KMFC.

$$\ln q_e = -\beta\varepsilon^2 + \ln q_m \tag{8}$$

$$\varepsilon = \mathrm{RT}\ln\left(1 + \frac{1}{c_e}\right) \tag{9}$$

$$\mathrm{E} = \frac{1}{\sqrt{2\beta}} \tag{10}$$

where c_e(mg L^{-1}) is the Pb (II) equilibrium concentration; q_e and q_{max}(mg g^{-1}) are the adsorption quantity at adsorbed equilibrium and the theoretical maximum adsorption amount, respectively; K_L(L mg^{-1}) and K_F((mg g^{-1})·(L mg^{-1})$^{1/n}$) are the Langmuir and the Freundlich constant, respectively; 1/n is the heterogeneity factor; K_T(L mg^{-1}) is the equilibrium binding constant, b_T is the Temkin isotherm constant, q_m (mg g^{-1}) is the theoretical isotherm saturation amount, β(mol^2 kJ^{-2}) and ε are the Dubinin–Radushkevich isotherm constant, R (8.314 J·mol^{-1}·K^{-1}) is the universal gas constant, T(K) is the Kelvin temperature, and E is the free energy.

All isotherms showed a similar shape and were nonlinear under a wide range of aqueous solution equilibrium concentrations (Fig. 5). The fitting constants and correlation coefficients (R^2) were both summarized in Table 3. The data for the Pb(II) adsorption quantity at adsorbed equilibrium(q_e, mg g^{-1}) and equilibrium concentration (C_e, mg L^{-1}) were well-fitted to the Langmuir isotherm model($R^2 > 0.994$), which signified that Pb(II) adsorption onto the KMFC was monolayer molecular adsorption (Xin et al., 2012). In addition, a notable characteristic of the Langmuir adsorption isotherm could be represented by the separation constant R_L^2, $R_L = 1/(1 + c_0 b)$ (CRINI et al., 2007). The R_L^2 values were 0.9947–0.9983, which verified that the shape of the isotherms was favorable ($0 < R_L^2 < 1$) (Bulut et al., 2008).

According to the Langmuir model, the maximum adsorption capacity of Pb (II) was 1075.27 mg g^{-1} on KMFC, which was similar to the calculated q_e (1085.78 mg g^{-1}) of the pseudo-second-order kinetic model. Compared with other reported sorbents, the adsorption capacity of Pb(II) on KMFC was far higher than any other sorbents (Alqadami et al., 2019; Lin et al., 2011; Liu et al., 2011; Xin et al., 2012; Xu et al., 2013) (Table 4). These comparisons confirmed that KMFC had a surprisingly excellent adsorption capacity, which fully demonstrated its adsorption advantages.

On the basis of the correlation coefficients in Table 3, Temkin model ($R^2 > 0.992$) could also fit the adsorption process well. The Temkin isotherm model assumes an indirect interaction between adsorbates and sorbents and describes this chemisorption using principal electrostatic interactions (Fan et al., 2017). The molecular heat of the adsorption decreases linearly with increases in coverage (Dil et al., 2017). From the table, the correlation coefficient (R_T^2) of Temkin adsorption isotherm was > 0.985, which was superior to the Freundlich adsorption isotherm ($R_F^2 > 0.902$) and D-R isotherm models ($R^2 > 0.795$). Thus, electrostatic interaction was an important mechanism between the Pb(II) and KMFC, which was consistent with the result of the pH influence.

In summary, the above fitting results revealed that the linear correlation coefficient of the Langmuir and the Temkin isotherm models were higher than the others. Hence, the KMFC involved uniform monolayer adsorption and electrostatic interactions for the removal of Pb(II). It was further indicated that the adsorption process may be caused by ion exchange adsorption to Pb(II) on the surface of the sorbent, or electrostatic adsorption to Pb(II), due to the negative charge on the surface of the sorbent, rather than physical adsorption as determined by van der Waals forces.

3.4. Adsorption thermodynamics for Pb(II)

It is critical to calculate the thermodynamic parameters, as they elucidate the thermodynamic changes during the adsorption process. (Ali et al., 2016). The thermodynamic theory assumes that entropy change is the driving force behind the inability to obtain and lose energy in isolated systems (Fan et al., 2011; Lei et al., 2017). At the same equilibrium concentration, the quantity of adsorbed Pb(II) increased with higher temperatures, which indicated that an elevated temperature was beneficial to the adsorption process.

Table 3 Constants and correlation coefficients of adsorption isotherms.

Temperature/K	Langmuir model			Freundlich model			
	q_m/(mg/g)	K_L/(L/mg)	R_L^2	K_F/(L/g)	n		R_F^2
298	1075.27	0.04021	0.9947	202.6135	3.5932		0.9293
308	1111.11	0.04663	0.9978	232.4790	3.8241		0.9028
318	1123.60	0.06168	0.9983	271.1033	4.1237		0.9203
Temperature/K	Temkin model			D-R model			
	b_T	K_T /(L/mg)	R_T^2	q_m /(mg/g)	B (mol^2 /kJ^2)	E (J)	$R_{D\text{-}R}^2$
298	15.7337	1.5065	0.9924	812.53	0.000003	408.248	0.7951
308	16.7113	2.3053	0.9850	870.36	0.000002	500.000	0.8771
318	18.3549	4.5159	0.9937	866.45	0.000001	707.407	0.8045

Table 4 Comparison of maximal reported adsorption capacity of Pb(II) removal with various adsorbents.

Name	Structure	BET (m^2/g)	Pore volume (cm^3/g)	q_e (mg/g)	pH_{pzc}	References
KMFC	Mesoporous, cubic lattice structure	42.24	0.18	1075.27	None, always negative	This study
Amine-functionalized mesoporous Fe_3O_4 (AF-Fe_3O_4)	Mesoporous	25.94	0.18	369.0	4.0	Xin et al., 2012
Titania–silica–phosphonate (TSP)	Mesoporous, semicrystalline anatase structure	670	1.1	92.40	–	Lin et al., 2011
Fe_3O_4@TATS@ATA	Mesoporous, nanocomposite	114	0.054	205.2	5.3	Alqadami et al., 2019
Iron oxide magnetic nanoparticles (MNPs) and Ca–alginate	–	–	–	188.25	–	Xu et al., 2013
Pb(II) ion-imprinted polymer (Pb(II)-IIP)	Mesoporous	113.81	0.27	38.10	–	Liu et al., 2011

Table 5 Thermodynamic data for the adsorption of Pb(II).

Temperature (K)	△G ($\times10^3$J·mol^{-1})	△H ($\times10^3$J·mol^{-1})	△S (J·mol^{-1}·K^{-1})
298	−22.367	16.793	131.212
308	−23.497		
318	−24.999		

Thermodynamic parameters such as Gibbs free energy (ΔG^0, J·mol^{-1}), enthalpy change (ΔH^0, J·mol^{-1}), and entropy change (ΔS^0, J·mol^{-1}·K^{-1}) are calculated according to Eqs. (11)–(13).

$$\Delta G^0 = -RTlnK_d \tag{11}$$

$$lnK_d = \frac{\Delta S^0}{R} - \frac{\Delta H^0}{RT} \tag{12}$$

$$\Delta G^0 = \Delta H^0 - T\Delta S^0 \tag{13}$$

where K_d(L mol^{-1}) is the apparent equilibrium constant, which is transformed from the Langmuir isotherm constant K_L.

Combined with the Langmuir isothermal equation, the specific analytical results were listed in Table 5. The negative value of ΔG^0 indicated that the Pb(II) adsorption process onto the KMFC was spontaneous. And, the ΔG^0 value decreased slightly, with the temperature increased, indicating that high temperatures were beneficial for the adsorption process. The positive value of ΔH manifested that the Pb(II) adsorption onto KMFC was an endothermic process, whereas the positive value of ΔS signified that the degree of chaos was increased during the Pb(II) adsorption process.

3.5. Adsorption mechanisms

Based on the above discussion, the mechanism of Pb(II) removal may involve electrostatic attraction and chemisorption (ion exchange). To further demonstrate this, Fourier-transform infrared spectroscopy (FTIR) and X-ray photoelectron spectroscopy (XPS) characterizations were confirmed.

The FTIR spectrum of KMFC in the range of 4000–450 cm^{-1} was depicted in Fig. 6a and the typical functional groups are shown in Table S1. The peaks of the primary KMFC functional groups included 3433.03 cm^{-1} (O—H stretching), 2068.17 cm^{-1} (C≡N stretching), 1629.30 cm^{-1} (O—H bending), 594.06 cm^{-1} (Fe—CN stretching) (Wang et al.), and 452.76 cm^{-1} (Mn—CN stretching). Several peaks were altered when the Pb(II) was adsorbed to the KMFC, including 3433.03 → 3468.63 cm^{-1}, 2068.17 → 2040.43 cm^{-1}, 1629.30 → 1617.32 cm^{-1}, 594.06 → 596.18 cm^{-1}, 452.76 → 453.92 cm^{-1}. Therefore, the lead ions occupied interstitial cavities within the cubic lattice of the KMFC, which did not affect the basic structure (Guo et al., 2018).

To further determine the KMFC surface chemistry, XPS analyses were conducted. As shown in Fig. 6, the main elemental composition prior to adsorption included Fe, Mn, C, N, K, and O. Once the adsorption was completed, Pb4f appeared on the full spectrum (Fig. 6b), which signified that Pb was adsorbed to the KMFC. The XPS spectrum of Pb 4f was fitted to the peaks, as shown in Fig. 6d. It can be seen that there were two peaks Pb $4f_{5/2}$ (142.96 eV) and Pb $4f_{7/2}$ (137.72 eV), which corresponded to Pb (II) (Wang et al., 2015). This revealed that the adsorption of Pb(II) by KMFC did not alter the valence of Pb. A plausible mechanism for the lead adsorption was that the negative KMFC surface facilitated the attraction of positively charged cations. The lead was adsorbed by KMFC started with electrostatic attraction, and then exchanged with potassium in the KMFC, that was evidenced via XPS, by the absence of the potassium peak following adsorption (Fig. 6b). Lead ions could easily enter the KMFC to be exchanged with potassium within the crystal lattice to achieve adsorption, due to the defect void structure of the KMFC (Shao et al., 2019; Xie et al., 2019a).

To further demonstrate the exchange of lead and potassium ion in solution, a supplementary experiment was performed as described below, with the results shown in Fig. 7. The concentration of Pb(II) in the solution began to decline to equilibrium over time, while potassium ions began to increase to equilibrium. Moreover, changes in the amount of substance of lead ions were smaller than those of potassium ions (Fig. 7b), i.e. $\Delta n(Pb^{2+}) < \Delta n(K^+)$, rather than $\Delta n(Pb^{2+}) = 2\Delta n(K^+)$.This undoubtedly confirmed the existence of an ion-exchange mechanism (K^+ exchange) during the adsorption process, where ion exchange was dominant, though not the only mechanism involved.

3.6. Stability and recyclability of KMFC in the present system

The effect of pH on adsorption is extremely large, as it affects the surface charge and functional groups of the sorbent, even the morphology of metal ions in solution (Kołodyńska et al., 2012). The result (Fig. S2) shown that the quantity of Pb(II) adsorption decreased as the pH increased. Meanwhile, the experiment found that the morphology of the KMFC did not change significantly (Fig. S3) while keeping in strong acid and alkali for 5 h. It also can be seen from the FTIR spectrum (Fig. S4), the chemical structure of KMFC did not change at pH = 2 or pH = 10, which proved the great pH stability of KMFC. Also, a cycling experiment was conducted in this study. A mixture of metal salts (0.5 M KCl and $MnCl_2$) was used as a desorption agent under batch conditions, due to the ion exchange of lead onto KMFC. It can be seen in Fig. S5 that after three cycles, the adsorbed quantity of KMFC was kept in 804.68 mg g-1, which was still higher than many other sorbents (Lin et al., 2011; Xu et al., 2013). Therefore, the KMFC was a promising highly-efficient and recyclable sorbent for the removal of Pb(II) from wastewater.

4. Conclusions

For this study, an efficient K-rich Prussian blue analogue sorbent, referred to as KMFC, was facilely synthesized and employed for the first time to remove Pb(II) from aqueous solutions. The preparation procedure of KMFC was simple, cost-effective, and environmentally compatible. The adsorption of Pb(II) onto the KMFC attained equilibrium within 180 min. at pH 5.0 and agreed well with the pseudo-second-order kinetic model, as well as the Langmuir and Temkin adsorption isotherm models. The maximum adsorption capacity of the KMFC for Pb(II) was 1075.27 mg g^{-1} at room temperature, which was significantly higher than any other reported materials. According to thermodynamic analyses,

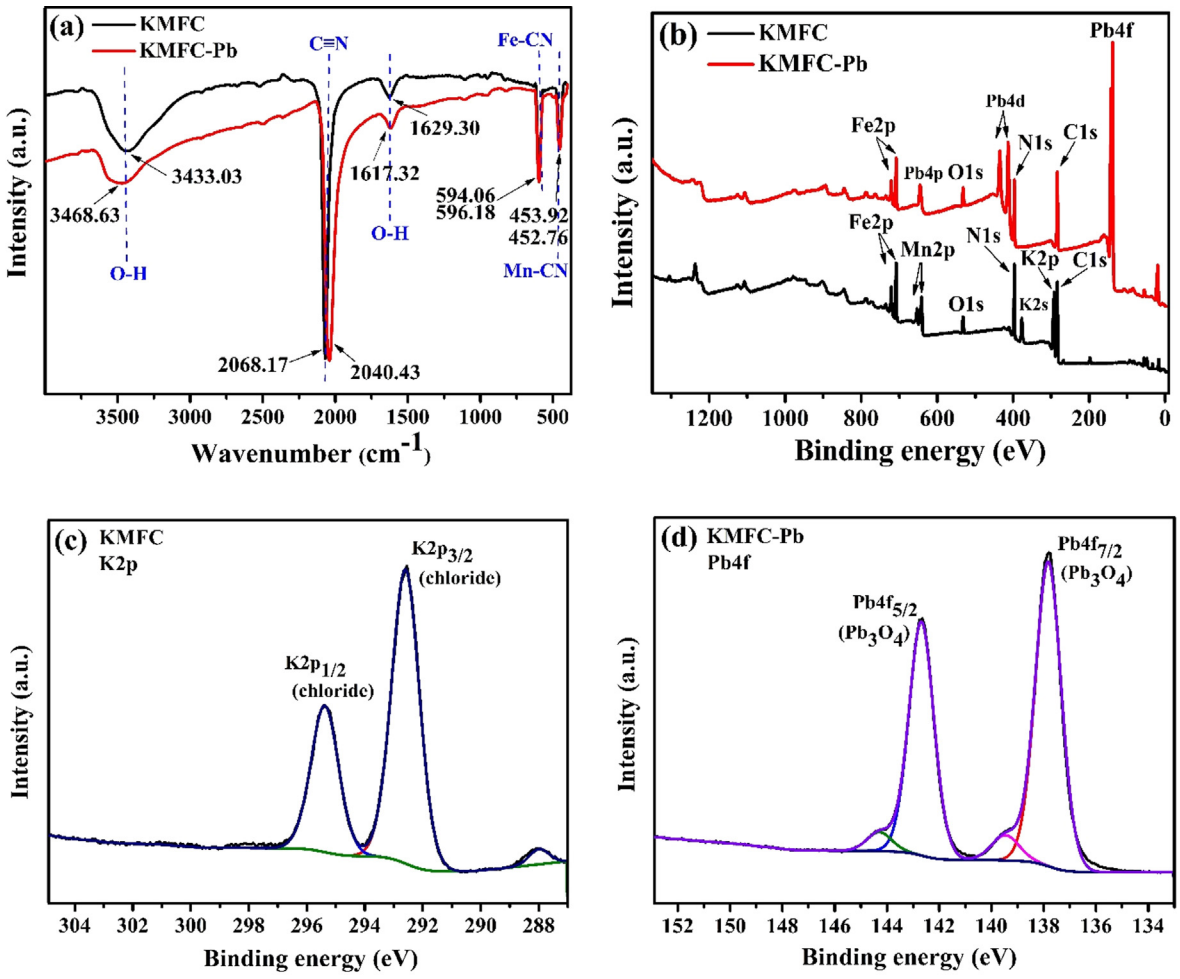

Fig. 6 FT-IR spectra of the KMFC (a); XPS of the pristine KMFC and following the adsorption of Pb(II) by KMFC: the full-survey spectrum (b), K2p(c), and Pb4f (d).

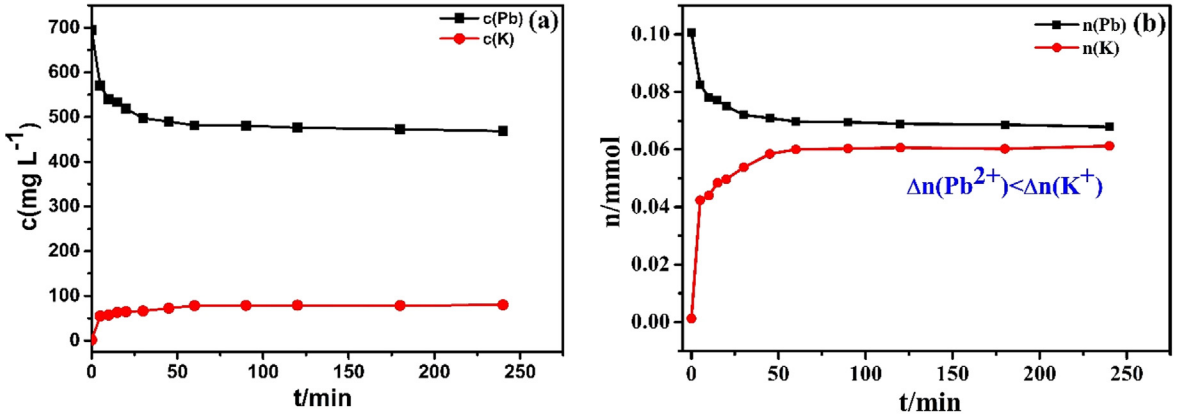

Fig. 7 Comparison of Pb(II) and K(I) during the adsorption (30 mL Pb(II) of 800 mg L^{-1},10 mg KMFC, pH = 5.0, 220 rpm, 0–4 h): concentration changes of Pb(II) and K(I) (a), comparison of the amount of substance of Pb(II) and K(I) (b).

the adsorption process was endothermic and spontaneous. The mechanism of Pb(II) adsorption involved electrostatic attraction and ion exchange, among which ion exchange was dominant. It is anticipated that this K-rich Prussian blue analogue will have broad applicability and efficiency for the removal of lead ions from wastewater.

Declaration of Competing Interest

The authors declare that they have no known competing financial interests or personal relationships that could have appeared to influence the work reported in this paper.

Acknowledgments

This work was financially supported by the National Science and Technology plan Project of China (2018-281), Guangdong Provincial Science and the Technology Plan Project (No. 2017A020216010), National Science Foundation for Young Scientists of China (Grant No. 21906029) and China Postdoctoral Science Foundation (Grant No. 2019T120102).

Appendix A. Supplementary material

Supplementary data to this article can be found online at https://doi.org/10.1016/j.arabjc.2020.02.022.

References

Alamudy, H.A., Cho, K., 2018. Selective adsorption of cesium from an aqueous solution by a montmorillonite-prussian blue hybrid. Chem. Eng. J. 349, 595–602.

Ali, R.M., Hamad, H.A., Hussein, M.M., Malash, G.F., 2016. Potential of using green adsorbent of heavy metal removal from aqueous solutions: Adsorption kinetics, isotherm, thermodynamic, mechanism and economic analysis. Ecol. Eng. 91, 317–332.

Alqadami, A.A., Naushad, M., Alothman, Z.A., Alsuhybani, M., Algamdi, M., 2019. Excellent adsorptive performance of a new nanocomposite for removal of toxic Pb(II) from aqueous environment: Adsorption mechanism and modeling analysis. J. Hazard. Mater. 121896.

Benhamou, A., Baudu, M., Derriche, Z., Basly, J.P., 2009. Aqueous heavy metals removal on amine-functionalized Si-MCM-41 and Si-MCM-48. J. Hazard. Mater. 171, 1001–1008.

Bulut, E., Ozacar, M., Sengil, I.A., 2008. Adsorption of malachite green onto bentonite: Equilibrium and kinetic studies and process design. Micropor. Mesopor. Mater. 115, 234–246.

Chen, R., Yu, J., Xiao, W., 2013. Hierarchically porous MnO2 microspheres with enhanced adsorption performance. J. Mater. Chem. A 1, 11682–11690.

Crini, G., Peindy, H.N., Gimbert, F., Robert, C., 2007. Removal of C. I. Basic Green 4 (Malachite Green) from aqueous solutions by adsorption using cyclodextrin-based adsorbent: Kinetic and equilibrium studies. Sep. Purification Technol. 53, 97–110.

Cui, H., Zhang, X., Li, Y., Chen, D., Zhang, Y., 2019a. First-principles insight into Ni-doped InN monolayer as a noxious gases scavenger. Appl. Surf. Sci. 494, 859–866.

Da'Na, E., Sayari, A., 2012. Adsorption of heavy metals on amine-functionalized SBA-15 prepared by co-condensation: Applications to real water samples. Desalination 285, 62–67.

Dan, C., Yang, L., Jia, Z., Li, W., Zhou, J., Li, S., Qian, G., 2012. Efficient removal of dyes by a novel magnetic Fe3O4 /ZnCr-layered double hydroxide adsorbent from heavy metal wastewater. J. Hazard. Mater. 243, 152–160.

Dil, E.A., Ghaedi, M., Asfaram, A., Hajati, S., Mehrabi, F., Goudarzi, A., 2017. Preparation of nanomaterials for the ultrasound-enhanced removal of Pb2+ ions and malachite green dye: Chemometric optimization and modeling. Ultrason. Sonochem. 34, 677–691.

Efome, J.E., Rana, D., Matsuura, T., Lan, C.Q., 2018. Metal-organic frameworks supported on nanofibers to remove heavy metals. J. Mater. Chem. A 6, 4550–4555.

Fan, J., Cai, W., Yu, J., 2011. Adsorption of N719 dye on anatase TiO2 nanoparticles and nanosheets with exposed (001) facets: equilibrium, kinetic, and thermodynamic studies. Chem. Asian J. 6, 2481–2490.

Fan, S., Yi, W., Yang, L., Tang, J., Zhen, W., Jie, T., Li, X., Kai, H., 2017. Facile synthesis of tea waste/Fe3O4 nanoparticle composite for hexavalent chromium removal from aqueous solution. RSC Adv. 7, 7576–7590.

Guo, S.Y., Liang, Y.L., Tricard, S., Wang, N., Feng, L., He, S.F., Zheng, P.Z., Zhao, J.H., Fang, J., 2018. Effect of cesium ion on the synthesis and catalytic properties with FeCo Prussian blue analogue. Chem. Phys. Lett. 710, 180–187.

Hao, Cui, Guozhi, Zhang, Xiaoxing, Zhang, Tang, J. Rh-doped MoSe 2 as a toxic gas scavenger: a first-principles study. 1.

Jiang, X., Zhang, T.R., Yang, L.Q., Li, G.C., Lee, J.Y., 2017. A Fe/Mn-Based Prussian Blue Analogue as a K-Rich Cathode Material for Potassium-Ion Batteries. Chemele. 4, 2237–2242.

Kang, S.-M., Rethinasabapathy, M., Hwang, S.K., Lee, G.-W., Jang, S.-C., Kwak, C.H., Choe, S.-R., Huh, Y.S., 2018. Microfluidic generation of Prussian blue-laden magnetic micro-adsorbents for cesium removal. Chem. Eng. J. 341, 218–226.

Kołodyńska, D., Wnętrzak, R., Leahy, J.J., Hayes, M.H.B., Kwapiński, W., Hubicki, Z., 2012. Kinetic and adsorptive characterization of biochar in metal ions removal. Chem. Eng. J. 197, 295–305.

Lei, C., Zhu, X., Zhu, B., Jiang, C., Le, Y., Yu, J., 2017. Superb adsorption capacity of hierarchical calcined Ni/Mg/Al layered double hydroxides for Congo red and Cr(VI) ions. J. Hazard. Mater. 321, 801–811.

Lin, X.Z., Ma, T.Y., Yuan, Z.Y., 2011. Titania–silica–phosphonate triconstituent hybrid mesoporous materials as adsorbents in gas and liquid phases. Chem. Eng. J. 166, 1144–1151.

Liu, Y., Liu, Z., Gao, J., Dai, J., Han, J., Wang, Y., Xie, J., Yan, Y., 2011. Selective adsorption behavior of Pb(II) by mesoporous silica SBA-15-supported Pb(II)-imprinted polymer based on surface molecularly imprinting technique. J. Hazard. Mater. 186, 197–205.

Maleki, A., Hayati, B., Naghizadeh, M., Joo, S.W., 2015. Adsorption of hexavalent chromium by metal organic frameworks from aqueous solution. J. Ind. Eng. Chem. 28, 211–216.

Manawi, Y., McKay, G., Ismail, N., Fard, A.K., Kochkodan, V., Atieh, M.A., 2018. Enhancing lead removal from water by complex-assisted filtration with acacia gum. Chem. Eng. J. 352, 828–836.

Mohan, S., Kumar, V., Singh, D.K., Hasan, S.H., 2017. Effective removal of lead ions using graphene oxide-MgO nanohybrid from aqueous solution: Isotherm, kinetic and thermodynamic modeling of adsorption. J. Environ. Eng. 5, 2259–2273.

Safruk, A.M., Mcgregor, E., Aslund, M.L.W., Cheung, P.H., Pinsent, C., Jackson, B.J., Hair, A.T., Lee, M., Sigal, E.A., 2017. The influence of lead content in drinking water, household dust, soil, and paint on blood lead levels of children in Flin Flon, Manitoba and Creighton, Saskatchewan. Sci. Total Environ. 593–594, 202–210.

Shao, P., Ding, L., Luo, J., Luo, Y., You, D., Zhang, Q., Luo, X., 2019. Lattice-Defect-Enhanced Adsorption of Arsenic on Zirconia Nanospheres: A Combined Experimental and Theoretical Study. ACS Appl. Mater. Interfaces 11, 29736–29745.

Sharma, G., Naushad, M., Al-Muhtaseb, A.H., Kumar, A., Khan, M. R., Kalia, S., Bala, M., Sharma, A., 2017. Fabrication and characterization of chitosan-crosslinked-poly(alginic acid) nanohydrogel for adsorptive removal of Cr(VI) metal ion from aqueous medium. Int. J. Biol. Macromol. 95. S0141813016315653.

Song, M., Wei, Y.X., Cai, S.P., Yu, L., Zhong, Z.P., Jin, B.S., 2018. Study on adsorption properties and mechanism of Pb2+ with different carbon based adsorbents. Sci. Total Environ. 618, 1416–1422.

Sun, Y.B., Ding, C.C., Cheng, W.C., Wang, X.K., 2014. Simultaneous adsorption and reduction of U(VI) on reduced graphene oxide-supported nanoscale zerovalent iron. J. Hazard. Mater. 280, 399–408.

Tiwari, J.N., Mahesh, K., Le, N.H., Kemp, K.C., Timilsina, R., Tiwari, R.N., Kim, K.S., 2013. Reduced graphene oxide-based hydrogels for the efficient capture of dye pollutants from aqueous solutions. Carbon 56, 173–182.

Wang, P., Du, M., Zhu, H., Bao, S., Yang, T., Zou, M., 2015. Structure regulation of silica nanotubes and their adsorption behaviors for heavy metal ions: pH effect, kinetics, isotherms and mechanism. J. Hazard. Mater. 286, 533–544.

Wang, Q., He, S., Wang, N., Zhao, J., Fang, J., Shen, W., Synthesis of CoFe Prussian blue analogue/carbon nanotube composite material and its application in the catalytic epoxidation of styrene. New J. Chem.

Xiao, F., Fang, L.P., Li, W.T., Wang, D.S., 2015. One-step synthesis of aluminum magnesium oxide nanocomposites for simultaneous removal of arsenic and lead ions in water. RSC Adv. 5, 8190–8193.

Xie, Y., Chen, C., Lu, X., Luo, F., Wang, C., Alsaedi, A., Hayat, T., 2019a. Porous NiFe-oxide nanocubes derived from prussian blue analogue as efficient adsorbents for the removal of toxic metal ions and organic dyes. J. Hazard Mater. 379, 120786.

Xie, Y., Chen, C., Ren, X., Tan, X., Song, G., Chen, D., Alsaedi, A., Hayat, T., 2019b. Coupling g-C3N4 nanosheets with metal-organic frameworks as 2D/3D composite for the synergetic removal of uranyl ions from aqueous solution. J. Colloid Interface Sci. 550, 117–127.

Xin, X., Qin, W., Jian, Y., Yan, L., Rui, F., Chen, G., Du, B., He, L., 2012. Highly efficient removal of heavy metal ions by amine-functionalized mesoporous Fe3O4 nanoparticles. Chem. Eng. J. 184, 132–140.

Xu, Zeng, Hu, Huang, 2013. Synthesis of iron oxide nanoparticles and their application in;Phanerochaete chrysosporium immobilization for Pb(II) removal. Colloids Surfaces A: Physicochem. Eng. Aspects 419, 147–155.

Xue, X., Jiang, X., Baig, S.A., Xu, X., 2016. Synthesis of graphene oxide nanosheets for the removal of Cd(II) ions from acidic aqueous solutions. J. Taiwan Instit. Chem. Eng. 59, 365–372.

Yan, Y., An, Q., Xiao, Z., Wei, Z., Zhai, S., 2017. Flexible core-shell/bead-like alginate@PEI with exceptional adsorption capacity, recycling performance toward batch and column sorption of Cr (VI). Chem. Eng. J. 313, 475–486.

Zhou, X.H., Zhou, J.J., Liu, Y.C., Guo, J., Ren, J.L., Zhou, F., 2018. Preparation of iminodiacetic acid-modified magnetic biochar by carbonization, magnetization and functional modification for Cd (II) removal in water. Fuel 233, 469–479.

Zhu, K., Chen, C., Xu, M., Chen, K., Tan, X., Wakeel, M., Alharbi, N.S., 2018. In situ carbothermal reduction synthesis of Fe nanocrystals embedded into N-doped carbon nanospheres for highly efficient U(VI) adsorption and reduction. Chem. Eng. J. 331, 395–405.